

Electronic transport and conduction mechanism transition in $\text{La}_{1/3}\text{Sr}_{2/3}\text{FeO}_3$ thin films

R. C. Devlin, A. L. Krick, R. J. Sichel-Tissot, Y. J. Xie, and S. J. May^{a)}

Department of Materials Science and Engineering, Drexel University, Philadelphia, Pennsylvania 19104, USA

(Received 15 April 2014; accepted 3 June 2014; published online 17 June 2014)

We report on the electronic transport properties of epitaxial $\text{La}_{1/3}\text{Sr}_{2/3}\text{FeO}_3$ films using temperature dependent resistivity, Hall effect, and magnetoresistance measurements. We show that the electronic phase transition, which occurs near 190 K, results in a change in conduction mechanism from nonadiabatic polaron transport at high temperatures to resistivity behavior following a power law temperature dependence at low temperatures. The phase transition is also accompanied by an abrupt increase in apparent mobility and Hall coefficient below the critical temperature (T^*). We argue that the exotic low temperature transport properties are a consequence of the unusually long-range periodicity of the antiferromagnetic ordering, which also couples to the electronic transport in the form of a negative magnetoresistance below T^* and a sign reversal of the Hall coefficient at T^* . By comparing films of differing thicknesses, stoichiometry, and strain states, we demonstrate that the observed conduction behavior is a robust feature of $\text{La}_{1/3}\text{Sr}_{2/3}\text{FeO}_3$. © 2014 AIP Publishing LLC. [<http://dx.doi.org/10.1063/1.4883541>]

I. INTRODUCTION

Interest in electronic phase transitions (EPTs) has motivated considerable work focused on perovskite and other complex oxide systems,^{1–4} with substantial efforts aimed at understanding these transitions in epitaxial heterostructures,^{5–11} the material architecture of choice for electronic devices.^{12–15} Electronic transport measurements have been used extensively to identify EPTs, develop electronic phase diagrams, and to compare relative metrics of these transitions, such as the transition temperature (T^*) and the magnitude of a resistivity change, in different materials.^{16–20} However, the identification of the underlying conduction mechanisms in EPT materials is a lesser studied topic, though one that can play a critical role in developing a deeper understanding of materials that undergo less common transitions such as insulator-insulator transitions or those that lack a distinct change in structural symmetry across T^* .

One such system is $\text{La}_{1/3}\text{Sr}_{2/3}\text{FeO}_3$ (LSFO), which exhibits an abrupt discontinuity in resistivity (ρ) at $T^* \sim 190\text{--}200$ K but with insulating behavior ($d\rho/dT < 0$) on both sides of the transition.²¹ This EPT is attributed to the formation of a nominally charge-ordered state with a $3d_{111}$ periodicity.^{22–25} Simultaneous with the charge-ordering transition, the material undergoes a magnetic transition leading to an antiferromagnetic (AF) state with a $\uparrow\uparrow\uparrow\downarrow\downarrow$ spin structure also ordered along the [111] direction.^{25,26} However, the EPT is not accompanied by a change in crystal symmetry as is often observed in oxides with metal-insulator transitions, such as the $R\text{NiO}_3$ (R = rare earth) compounds, CaFeO_3 and the half-doped manganites,²⁷ although changes in the local Fe-O bonding environments have been observed.^{24,28} Instead, LSFO retains the rhombohedral $R\bar{3}c$ symmetry

across the transition, as determined from neutron diffraction measurements.²⁶ This lack of symmetry change, absence of metallic behavior above T^* , the critical role played by the magnetic ordering in the EPT,^{29,30} and the relatively long periodicity of the ordering separates the EPT in LSFO from that of other $3d$ perovskites and warrants closer examination of the transition.

One outstanding issue is the behavior of the carriers responsible for conduction. While multiple groups have reported on the resistivity change at T^* ,^{21,27,31–34} a detailed study of the conduction mechanisms in this material has yet to be put forth. Optical spectroscopy measurements have revealed the opening of a gap on the order of 0.15 eV below T^* .³⁵ This result motivates the questions: is conduction below T^* consistent with thermal activation of carriers across a gap; and, why is conduction non-metallic above T^* ?

In this work, we address these issues through an analysis of variable temperature resistivity measurements carried out on epitaxial LSFO films grown on $(\text{La,Sr})(\text{Al,Ta})\text{O}_3$ (LSAT) and SrTiO_3 (STO) substrates. At high temperatures, a strong electron-lattice coupling leads to nonadiabatic polaron conduction, resulting in the semiconducting behavior present above T^* despite the large number of carriers observed from the Hall coefficient. We show that the low temperature conduction is not consistent with activated behavior or conventional variable range hopping (VRH), but instead exhibits a power law dependence on temperature. Abrupt changes in the Hall coefficient, mobility, and magnetoresistance (MR) at T^* support our assignment of the conduction mechanism transition, while also pointing to the importance of the long-range periodicity of the antiferromagnetic order in electron transport. Finally, we show that the transport properties are consistent for films of different thickness, stoichiometry, and strain states, confirming that these results are intrinsic to LSFO and not due to extrinsic effects.

^{a)}Electronic mail: smay@coe.drexel.edu

II. SAMPLES AND EXPERIMENTAL METHODS

$\text{La}_{1/3}\text{Sr}_{2/3}\text{FeO}_3$ films were deposited on single crystal (001) LSAT and STO substrates using ozone-assisted ($\sim 5\%$ O_3 in O_2) molecular beam epitaxy (MBE) (Omicron modified LAB-10 system). These substrates induce a 0.1% compressive (LSFO on LSAT) and 0.9% tensile strain (LSFO on STO) into the films. The metal cations were co-evaporated using Knudsen cells containing elemental La, Sr, and Fe; shuttering of the sources was controlled using an Arduino program. During growth, the temperature was $600 \pm 25^\circ\text{C}$ at an ozone pressure of 2×10^{-6} Torr. Following the deposition, all samples were annealed in a tube furnace (Thermo Scientific Lindberg Blue M) at atmospheric pressure under flowing O_2 at 675°C for 3 h, immediately followed by an additional anneal under flowing O_2/O_3 (95/5%) at 200°C for 30 min. This two-step annealing process has proven to be an effective method to minimize oxygen vacancy concentrations in LSFO films^{36,37} as evidenced by low resistivity values at room temperature.

X-ray reflectivity (XRR) and diffraction were used to determine the film thickness and lattice parameters using a Rigaku Smartlab diffractometer. Cation composition was determined using Rutherford backscattering spectroscopy (RBS) measurements performed at the Laboratory for Surface Modification at Rutgers University. These measurements were performed on films grown on STO with a thickness of 60 unit cells or greater. In the case of thinner films or films grown on LSAT, the large substrate signal makes quantitative analysis of the RBS data difficult. The SIMNRA software was used to simulate the RBS spectra; the cation compositions were determined by minimizing the squared difference between the measured and simulated counts at each channel.³⁸ A list of the samples used in the study is presented in Table I.

In the case of AK22, which is the film discussed in Secs. III A and III B, synchrotron x-ray diffraction measurements were conducted at Sector 6-ID-B of the Advanced Photon Source using a photon energy of 10.0 keV. Figure 1 shows the diffracted intensity along the [00L] direction through the (001) reflections from the substrate and the film. The diffracted intensity was simulated using the GenX package to accurately determine the c -axis lattice parameter of the film.³⁹ The model indicates the film consists of 37 unit cells with an average c -axis parameter of $3.878 \pm 0.004 \text{ \AA}$.

TABLE I. Basic properties of the LSFO films used in this study. The thicknesses and compositions are determined from XRR and RBS measurements, respectively. Films on LSAT and ultrathin films on STO were not measured with RBS due to the difficulty in quantitatively analyzing the weak film signal over the large substrate signal.

Sample name	Substrate	Thickness (nm)	Measured cation composition
AK22	LSAT	15.1	...
RST172	STO	23.8	$\text{La}_{0.35}\text{Sr}_{0.65}\text{Fe}_{0.96}$
RST175	LSAT	13.8	...
RST176	STO	13.5	...
JD16	STO	39.9	$\text{La}_{0.38}\text{Sr}_{0.62}\text{Fe}_{0.99}$
AK42	STO	34.1	$\text{La}_{0.27}\text{Sr}_{0.65}\text{Fe}_{1.0}$

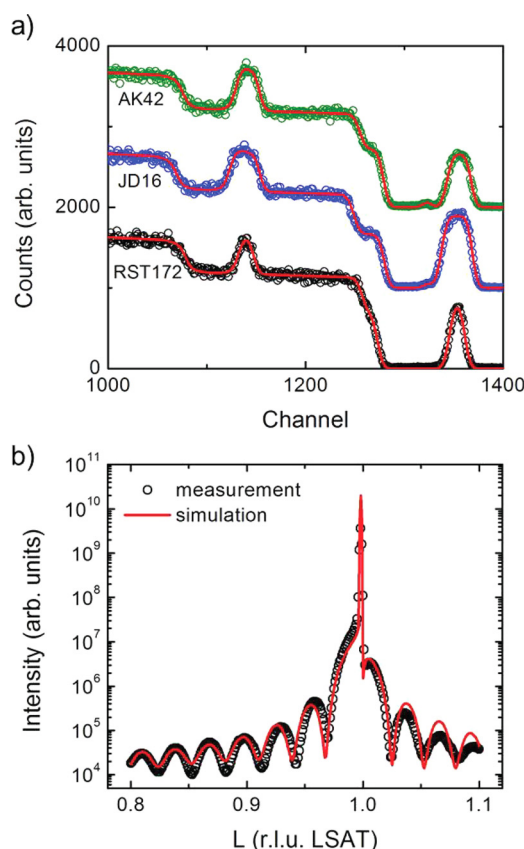


FIG. 1. Measured (open symbols) and simulated (red lines) RBS data (a); spectra are offset for clarity. Measured (open circles) and simulated (solid line) x-ray diffraction data from the (001) Bragg peak of sample AK22 (b).

The film is therefore under slight compressive strain, as the lattice parameter of LSAT is 3.868 \AA . The 1–2 unit cells of the LSFO at the film/substrate interface have slightly displaced cation positions and a modified c -axis parameter compared to the rest of the film, which is modeled as perfectly crystalline. Transverse scans at the film and substrate peaks confirm that the film is epitaxial and strained. The thickness obtained from x-ray reflectivity (39 unit cells) was used in calculating the carrier concentration, as reflectivity measures the total film thickness as opposed to the number of coherent crystallographic layers that contribute to diffraction.

Resistivity, Hall effect, and magnetoresistance (MR) measurements were carried out using a Physical Property Measurement System (PPMS) by Quantum Design. Resistivity was collected using standard four-point probe geometry, and contact to the sample was made with gold wire and silver paste. Current was sourced in both positive and negative directions to eliminate thermal voltages using a Keithley 6220 current source, and the resulting voltage was measured using a Keithley 2148 Nanovoltmeter. The T^* values were taken to be the local maximum of the second derivative of $\ln(\rho)$ with respect to temperature.⁴⁰ MR was collected with the magnetic field oriented parallel to the pseudocubic [001] of the LSFO film (out of plane direction). At fixed temperatures, the magnetic field was swept between -9 T and 9 T to check that the data was symmetric about the 0 T point. The MR is defined as

$$MR = \frac{R(9T) - R(0T)}{R(0T)}. \quad (1)$$

Hall effect was measured using a van der Pauw probe configuration. Due to the presence of magnetoresistance below the EPT in LSFO samples, which appears in series with Hall effect signal, the collected data were fit to a quadratic model with the linear portion of the fit used to determine the Hall coefficient.⁴¹

III. RESULTS AND DISCUSSION

A. Electronic transport above T^*

We start with a detailed description of the transport properties obtained from AK22, a sample chosen due to its similarity with previously reported resistivity data on stoichiometric bulk LSFO.²¹ All data presented in Secs. III A–III C were obtained from this sample. The temperature-dependent resistivity of this LSFO film is shown in Figure 2. At room temperature, LSFO exhibits a resistivity of approximately 2 mΩ cm. Over the range of 300 to 200 K there is little change in resistivity, with only a small increase as temperature decreases indicating the presence of semiconducting behavior. Below 200 K, the resistivity begins to increase more rapidly, and at $T^* = 188$ K, there is an abrupt jump in resistivity indicating an EPT. This phase transition increases the resistivity by an order of magnitude over a narrow temperature range of approximately 10 K. Resistivity measurements performed upon warming and cooling through the EPT reveal the presence of hysteresis, shown inset of Fig. 2. The thermal hysteresis points to a first order transition, consistent with previous reports of LSFO in bulk and thin film form.^{21,32,33}

Below the transition, the resistivity increases nearly seven orders of magnitude from T^* to 9 K, where the resistance reached the maximum measurable value of the measurement system. This large change in resistance is in stark contrast to the weakly insulating behavior above T^* and occurs over a similar temperature range. The change in the general behavior of resistivity data indicates that there is

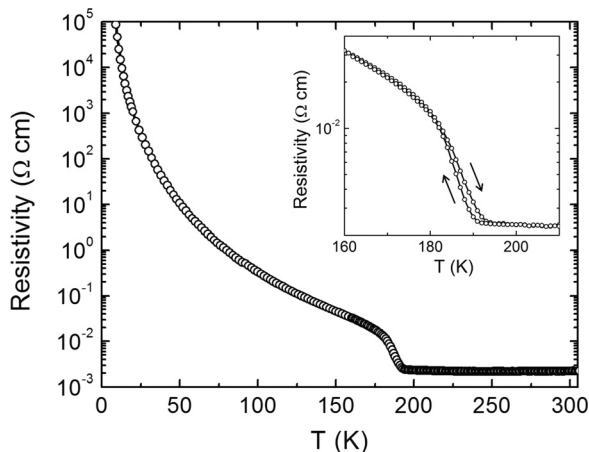


FIG. 2. Resistivity as a function of temperature for a LSFO film (AK22) grown on LSAT. The observed transition is at approximately 188 K. Inset shows a forward and back temperature sweep about T^* and the accompanying thermal hysteresis.

likely a transition in the underlying conduction mechanism above and below the EPT.

To elucidate the mechanisms responsible for electronic conduction in LSFO, the resistivity data was fit using a variety of models that describe electronic transport, including standard activated behavior, small polaron conduction in both the adiabatic and nonadiabatic limits,⁴² 3D VRH⁴³ and VRH considering electron-electron interactions.⁴⁴ At temperatures above T^* , the transport behavior is well fit by the conduction model of a small polaron hopping through the crystal lattice, given by^{42,45}

$$\rho = \rho_0 T^\alpha \exp\left(\frac{W_H}{k_B T}\right), \quad (2)$$

where W_H is the activation energy of the small polaron, α relates to the probability of the polaron to hop with each lattice vibration and is 1 for the adiabatic case and 3/2 for nonadiabatic polarons, k_B is Boltzmann's constant, and T is the absolute temperature. In the nonadiabatic model, the polaron binding energy (W_P) can be estimated as $W_P = 2W_H$ which is related to the electron-phonon coupling constant (γ) by⁴⁵

$$\gamma = \frac{W_P}{h\nu_0}, \quad (3)$$

where h is Planck's constant and ν_0 is the optical phonon frequency, approximated as 5.28×10^{12} Hz using linear extrapolation of data obtained by Tajima *et al.*⁴⁶ The fit to Eq. (2) is shown in Fig. 3 in the nonadiabatic limit ($\alpha = 3/2$). The fitting parameters for both the adiabatic and nonadiabatic models are given in Table II for sake of comparison as well as the quantities derived from the fitting parameters.

An important caveat on the Holstein model of thermally hopping small polarons is that the model is applicable for $T > \Theta_D/2 = h\nu_0/k_B$, where Θ_D is the Debye temperature.^{42,45} We are unaware of reports of either the optical phonon frequency or heat capacity for LSFO at this composition; therefore, the exact Θ_D is not known. However, the optical phonon frequency has been determined in $\text{La}_{1-x}\text{Sr}_x\text{FeO}_3$ for

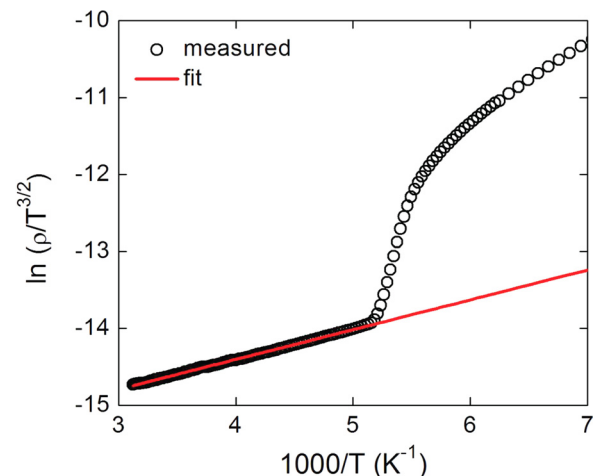


FIG. 3. Temperature-dependent resistivity for LSFO plotted in the nonadiabatic polaron model. The open circles show the measured data, and the solid line shows the fit to the nonadiabatic polaron model for $T > T^*$.

TABLE II. Summary of both adiabatic and nonadiabatic polaron fitting parameters and calculated physical quantities obtained from the nonadiabatic results.

Model	W_H (meV)	ρ_0 (Ω cm)	W_p (meV)	γ
Nonadiabatic	33	1.18×10^{-7}	66	3.0
Adiabatic	22	3.12×10^{-6}

$0 \leq x \leq 0.4$,⁴⁶ yielding $\Theta_D = 270$ K. Heat capacity measurements have been reported for $\text{La}_{0.5}\text{Sr}_{0.5}\text{FeO}_{2.9}$, yielding a Debye temperature of 416 K.⁴⁷ Thus, we conclude that the model is applicable for the temperatures over which the fit was performed ($T > T^*$).

Although the nonadiabatic polaron model provides the best fit to the data, the adiabatic model yielded fits that are nearly equivalent to the nonadiabatic case, consistent with several other reports in oxides.^{41,48} However, for LSFO, the nonadiabatic model is likely the applicable model. First, although the two models both fit the data well (for example, R^2 values of 0.99994 and 0.99983 were obtained for nonadiabatic and adiabatic models, respectively), in the film described here as well as the five other films presented in Sec. III D, the nonadiabatic model consistently provides the higher R^2 value. Second, the activation energies in the case of the nonadiabatic model are inherently higher whereas in some cases the adiabatic fits yield activation energies that are less than $k_B T$ down to temperatures of 250 K, implying $d\rho/dT > 0$, which is inconsistent with experimental observations. Finally, analysis including the experimentally determined mobilities, discussed in greater detail in Sec. III C, provides quantitative physical evidence for nonadiabatic processes.

A large number of perovskite oxides are known to exhibit polaron conduction, for instance $\text{La}_{0.7}\text{Ca}_{0.3}\text{MnO}_3$ ⁴⁹ and $\text{La}_{0.5}\text{Pb}_{0.5}\text{Mn}_{1-x}\text{Cr}_x\text{O}_3$.^{48,50} The already narrow bands of the e_g electrons, ionic nature of the lattice, and high dielectric constants makes perovskites susceptible to the self-trapping of small polarons.⁴⁵ In LSFO, the carrier responsible for the polarization of the lattice is expected to be a hole. This results from the fact that replacing La^{3+} in the parent compound LaFeO_3 with Sr^{2+} leads to a nominal shift in iron valence from $3+$ to $4+$, accompanied by a change in electron configuration from d^5 ($t_{2g}^3 e_g^2$) to d^4 ($t_{2g}^3 e_g^1$). This would be expected to result in approximately 0.67 holes/Fe at the composition of LSFO used in this study. The creation of small polarons explains why, despite such a high density of carriers in a partially filled e_g band, the conduction is not metallic. Instead, LSFO exhibits a low polaron activation energy, 33 meV, which is consistent with the weakly temperature-dependent resistivity in the high temperature phase.

Polaron conduction has been previously observed in insulating $\text{La}_{1-x}\text{Sr}_x\text{FeO}_3$ ($x \leq 0.3$)⁵¹ with activation energies of 0.53, 0.42, and 0.29 eV for $x = 0.05$, 0.20, and 0.30, respectively, as well as in $\text{La}_{1/3}\text{Sr}_{2/3}\text{FeO}_{2.88}$ for which $W_H = 70$ meV was reported.⁵² Both of these results point to the fact that the polaron activation energy is dependent on the carrier concentration since W_H decreases with increasing Sr doping. Similarly, an increase in the concentration of oxygen vacancies (which remove holes from the system) causes an increase in

activation energy. This trend of a continued decrease in activation energy with increasing hole concentration, along with the fact that LSFO has a relatively low electron-phonon coupling constant, $\gamma = 3.0$ compared to typical values in oxides of 4–9,^{45,48,53} and an activation energy on the order of $k_B T$, suggests that at the 0.67 holes/Fe, LSFO is close to a critical carrier density above which there is a transition to metallic conduction.^{54–56} Similar observations of critical carrier densities made in WO_{3-x} ,⁵⁵ $\text{NbO}_{2.5-x}$,⁵⁴ and $\text{La}_{2-x}\text{Sr}_x\text{CuO}_4$ ⁵⁶ have been explained as the carrier density equaling the number of sites at which small polarons can be formed.

B. Electronic transport below T^*

Contrary to the high temperature resistivity, the low temperature resistivity does not fit to the polaron model. To identify the low temperature conduction mechanism, the resistivity data were evaluated using the logarithmic derivative method, in which $\ln W$ is plotted against $\ln T$ with $W = -d(\ln\rho)/d(\ln T)$.^{57,58} The slope of this plot is the exponent m in the equation

$$\rho = \rho_0 \exp\left(\frac{T_0}{T}\right)^m, \quad (4)$$

where ρ_0 is a prefactor. In the case of simple activated behavior, $m = 1$ and $T_0 = E_A/k_B$, where E_A is the activation energy. The exponents $m = 0.5$, 0.33, and 0.25 indicate Efros-Shklovskii VRH, two-dimensional VRH, and three-dimensional VRH, respectively. As can be seen in Fig. 4(a), the logarithmic derivative analysis reveals a slope of $m = 0$. This exponent is indicative of non-exponential, power law behavior. The non-exponential nature of the transport can be further seen in Figs. 4(b) and 4(c) in which the failure of the activated and 3D VRH models to fit the resistivity data is shown. In contrast, the resistivity data can be fit with excellent agreement to a power law, $\rho = \rho_0 T^p$, dependence, as shown in Fig. 4(d). For the fit to AK22, a value of $p = -5.0$ is obtained.

The observation of power law, as opposed to exponential, resistivity behavior is unusual and indicates the presence of a novel transport mechanism below T^* . We attribute this exotic conduction behavior to the unusual spin structure present in the antiferromagnetic state, in which the ordering is $\uparrow\uparrow\downarrow\downarrow$ along [111], with the Neel temperature equal to T^* .^{25,26} We hypothesize that this spin structure plays a critical role in the transport. In the magnetically ordered state, the carrier must hop a minimum distance of $\sqrt{6}a$ in order to move between adjacent ferromagnetically coupled trilayers with the spin state conserved, as shown in Fig. 5. Additionally, thermal perturbation may cause spin fluctuations leading to longer hop distances, such as $\sqrt{8}a$, $3a$, or $\sqrt{11}a$. However, unlike the variable-range hopping scenario, there does not exist a continuous variation of hop distances, instead the hop distances are fixed by the magnetism.

We are unaware of a quantitative transport model developed to describe the conduction behavior hypothesized. However, we note that a power law resistivity dependence has been previously attributed to multiple phonon assisted

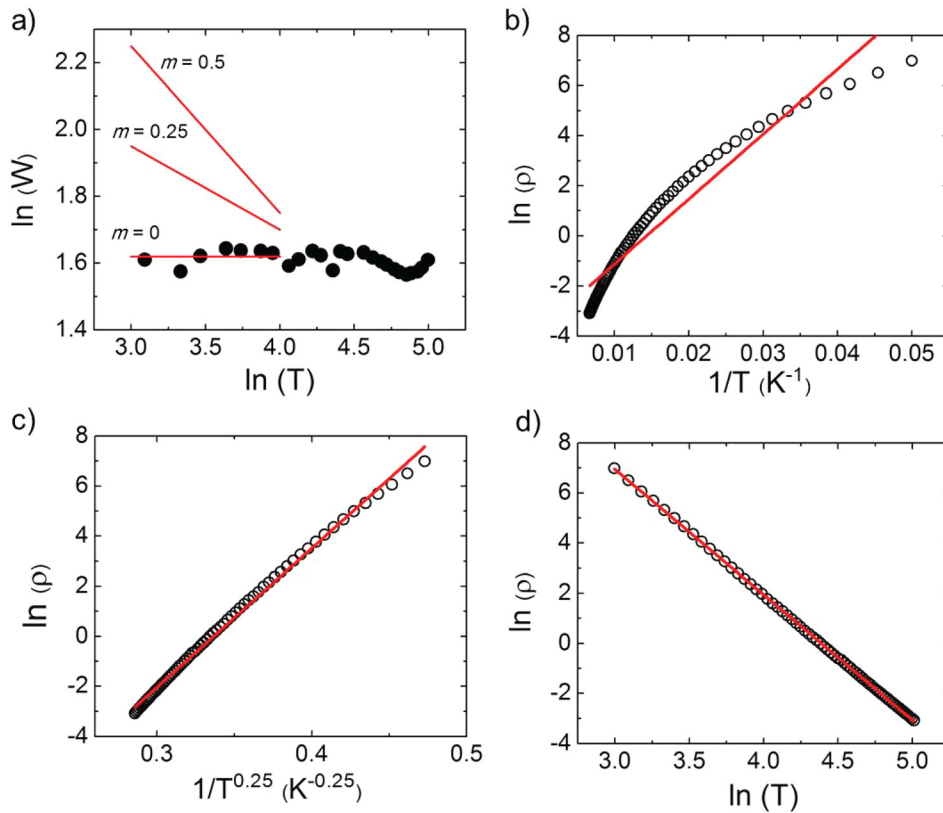


FIG. 4. Temperature-dependent resistivity evaluated from 20–150 K using the logarithmic method (a); slopes associated with 3D VRH ($m=0.25$) and E-S VRH ($m=0.5$) are shown for comparison. Fits to a simple activated model (b) and 3D VRH (c) fail to reproduce the data. Instead, the resistivity follows a non-exponential, power law dependence shown in (d).

hopping with reported values of p ranging from -3 to -17 .^{59–61} Given the electron-lattice coupling that yields polaron conduction above T^* , the power law behavior may indicate that the hopping between adjacent ferromagnetic layers is a multiple phonon assisted process. In this scenario, the large hopping distance due to the antiferromagnetic ordering likely requires the adsorption of energy from multiple phonons per carrier.

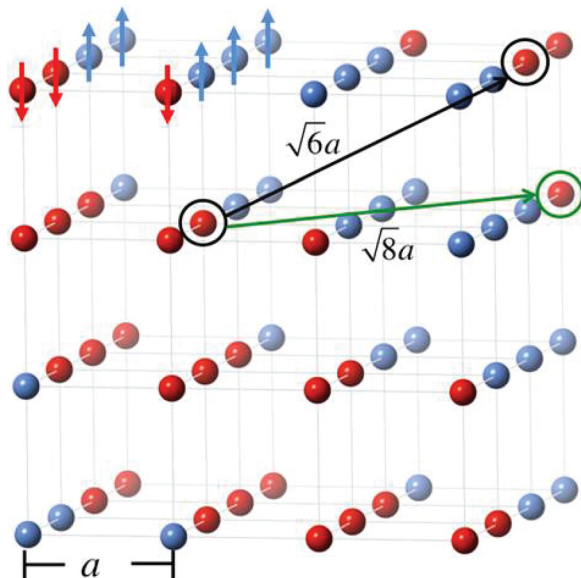


FIG. 5. A schematic of the Fe sublattice is shown in which blue and red spheres represent spin up and down states. The nearest hop distances between adjacent ferromagnetically coupled layers are highlighted.

C. Hall coefficient and magnetoresistance

Further verification of the conduction mechanisms was obtained through temperature dependent Hall effect measurements. The top panel of Fig. 6 shows the Hall coefficient (R_H) as a function of temperature for LSFO. In the high temperature phase, the sign of R_H indicates p-type conduction (holes). Above T^* , there is little change in R_H with decreasing temperature. The average high temperature carrier concentration obtained from R_H corresponds to 0.8 holes/u.c., close to the estimated Sr doping of 0.67 holes/u.c. As the temperature is decreased through T^* , the Hall coefficient increases sharply in magnitude and the sign of the Hall coefficient is inverted, consistent with previous reports of LSFO.³³ The sign inversion of R_H is consistent with our assignment of hopping conduction below T^* , as R_H sign inversion is often observed in hopping conductors.^{58,62,63} We also note that R_H sign inversion has been reported in other perovskites, coinciding with the onset of antiferromagnetic order.^{64,65}

The Hall mobilities (μ) were calculated using the relation $\rho = 1/ne\mu$. The calculated mobilities are shown in the bottom panel of Fig. 6. Above the transition, the mobilities are very low as is characteristic of many oxides exhibiting polaron conduction, with values between $0.1 \text{ cm}^2/\text{V s}$ and $0.2 \text{ cm}^2/\text{V s}$. Across the phase transition, there is an abrupt increase in mobility of about an order of magnitude, leading to $\mu = 1\text{--}2 \text{ cm}^2/\text{V s}$ below T^* . Here we note that below T^* , the mobility should be treated as an apparent mobility as a direct conversion from Hall coefficient to carrier concentration is not possible given the uncertainty regarding the exact nature of the novel conduction mechanism in the non-exponential transport regime. However, the increase in

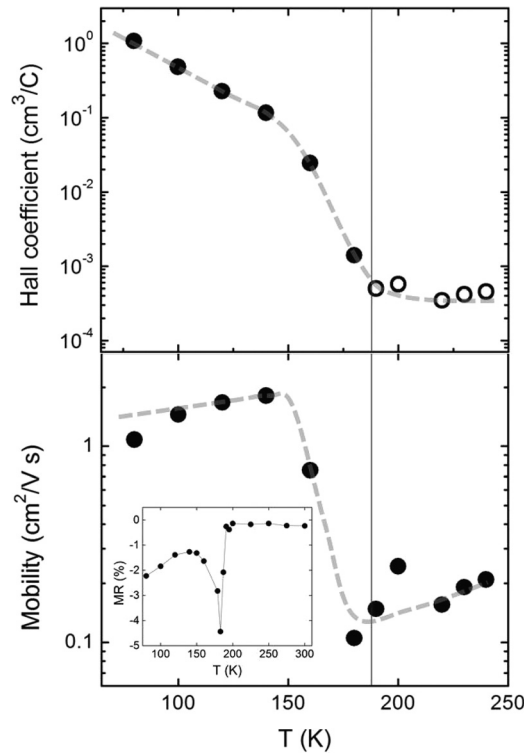


FIG. 6. (Top panel) Hall coefficient (top panel) and Hall mobility (bottom) as a function of temperature; the dashed lines are guides to the eye, while the solid line indicates T^* . The open symbols above 180 K correspond to p-type conduction as indicated by a positive Hall coefficient; the closed symbols below 180 K indicate a negative Hall coefficient. The magnetoresistance as a function of temperature is shown inset of the bottom panel.

apparent mobility across the transition likely occurs due to the switch in conduction mechanism, as hopping is less influenced by the increased effective mass associated with polaron formation.

In the high temperature phase, the near constant carrier concentration that corresponds very closely to the Sr doping can be explained in terms of the polaron model. Within the model of small polaron hopping, the activated behavior observed in resistivity data is a result of an activated mobility due to increased lattice vibrations at higher temperatures, not an activation of carriers.^{42,45} Thus, it is expected that the carrier concentration should remain constant above T^* in LSFO, as shown in the upper panel of Fig. 6.

The mobility data allows further investigation of the validity of the nonadiabatic polaron model. For a nonadiabatic polaron, the mobility varies with temperature as^{42,45}

$$\mu = \frac{3ea^2J^2}{2\hbar kT} \left(\frac{\pi}{4W_H kT} \right)^{1/2} \exp \left[-\frac{W_H}{k_B T} \right], \quad (5)$$

where J is the electron transfer integral. The nonadiabatic model is applicable when

$$J \ll J_{\max} = \left(\frac{2W_H k_B T}{\pi} \right)^{1/4} \left(\frac{\hbar\nu_0}{\pi} \right)^{1/2}. \quad (6)$$

While there can be differences between the Hall mobility and drift mobility for small polarons,⁴⁵ the value for Hall mobility obtained here and elsewhere³³ matches closely to

the drift mobility obtained from field-effect measurements.³³ Therefore, J can be approximated using Eq. (5) with $\mu = 0.15 \text{ cm}^2/\text{V s}$ at 190 K and $W_H = 33 \text{ meV}$. Although the precise optical phonon frequency is not known for LSFO, values between 10^{12} – 10^{13} Hz can be assumed so that J_{\max} can also be estimated. Carrying through such analysis gives values of J_{\max} ranging from 2.0–6.3 meV, whereas J is found to be only 0.03 meV. Thus, the condition in Eq. (6) is clearly satisfied as the calculated value of J derived from measured quantities is nearly two orders of magnitude less than the lower limit of J_{\max} , confirming that the nonadiabatic model is applicable.

Magnetoresistance measurements were performed to provide insight into the interplay between the magnetic ordering and electronic transport. The MR data as a function of temperature are shown inset of Figure 6. In the high temperature paramagnetic phase where polaron conduction is observed, the MR is negligible. At T^* , there is an abrupt increase in the magnitude of MR to its maximum value of -4.5% . Following the local maximum in magnitude, the MR begins to decrease in magnitude with decreasing temperature. At 140 K, the magnitude of MR reaches a local minimum of -1.5% after which, it increases monotonically with temperature. Within the fields used to measure the MR, -9 T to $+9 \text{ T}$, the MR is symmetric about $B = 0$ and does not saturate with field.

Magnetoresistance has previously been reported in polycrystalline and epitaxial LSFO.^{21,33} The data presented for single crystal films by Ueno *et al.*³³ are in close agreement with that in Fig. 6 over the temperature range presented from 300 to 150 K. The maximum in negative MR at T^* is likely a result of a field-induced suppression of the AF ground state, which slightly decreases the ordering temperature and T^* . The continued negative MR at low temperatures is attributed to a decrease in the hopping distance resulting from a suppression of spin disorder.

D. Effects of thickness, stoichiometry, and substrate

We now turn to temperature-dependent resistivity measured in the other five LSFO films to confirm that the change in conduction mechanism at T^* is a robust feature of LSFO, independent of thickness and slight deviations of stoichiometry. Figure 7 presents the resistivity as a function of temperature for these additional samples. All samples were fit to the conduction mechanisms described in Secs. III A and III B, both above and below T^* . Similar to AK22, the resistivity data in all the films were best fit to non-adiabatic polaron conduction above T^* and a power law dependence below T^* .⁶⁶ The T^* values and the obtained fitting parameters are given in Table III.

These results allow for the influence of thickness, substrate, and stoichiometry on the transport parameters to be disentangled. The effect of thickness can be seen by comparing RST176, RST172, and JD16, all of which are on STO. We note that RST176 was grown immediately following RST172 under the same conditions, and therefore, the cation composition of these two samples is assumed to be the same. In these three samples, there is minimal variation between

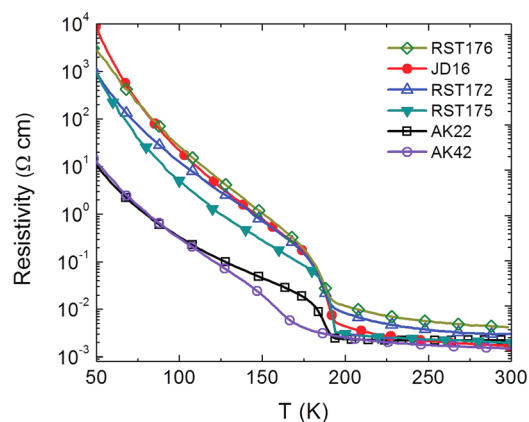


FIG. 7. Resistivity as a function of temperature for all six LSFO films.

T^* and W_H , indicating that there is little effect of sample thickness on the ordering temperature or polaron conduction over the thickness range studied here. Similarly, the T^* values of RST175 and RST176, samples grown simultaneously on STO and LSAT, are approximately the same, revealing the relative independence of the charge ordering transition to small amounts of tensile strain. The one parameter that appears sensitive to strain is the polaron activation energy, with the tensile strained acting to increase W_H . The two films grown on LSAT (AK22 and RST175) exhibit values of W_H that are less than those of the three nominally stoichiometric films on STO (RST172, RST176, and JD16) by roughly a factor of 2. Tensile strain nominally increases the in-plane Fe-O bond lengths leading to the observed higher activation energies.

The effect of cation site stoichiometry is more complex as it alters both the cation vacancy concentration due to non-stoichiometry and the nominal Fe valency. Assuming a fully oxygenated lattice, a nominal valence of 3.89, 3.84, and 3.66 is expected for the Fe cations in AK42, RST172, and JD16, respectively. The main difference between the three samples is the suppressed transition temperature, $T^* = 164$ K, of AK42. This coincides with both a significant A-site deficiency ($\sim 8\%$) and the largest nominal Fe valence. The polaron activation energy for this sample is also less than RST172 and JD16. In contrast, the presence of a 4% B-site deficiency in RST172 does not lead to a reduction in T^* . Finally, a general trend observed from all three films is that the magnitude of p decreases with increasing nominal Fe valence, which leads to increased hole doping.

TABLE III. Transition temperature and fitting parameters obtained from the LSFO films. The W_H and p values were determined from fitting resistivity data above T^* and below T^* , respectively.

Sample	T^* (K)	W_H (meV)	p
AK22	188	33	-5.0
RST172	188	84	-6.3
RST175	192	52	-7.3
RST176	190	83	-7.3
JD16	188	78	-8.3
AK42	164	59	-5.3

IV. CONCLUSIONS

The conduction mechanisms in $\text{La}_{1/3}\text{Sr}_{2/3}\text{FeO}_3$ have been investigated using variable temperature transport measurements, revealing a transition from nonadiabatic polaron conduction to an exotic transport mechanism with a non-exponential, power law temperature dependence as the sample is cooled through the electronic phase transition, resulting in an increase in the Hall coefficient and apparent mobility below T^* . We attribute the low temperature transport to the presence of hopping behavior arising from the long-periodicity of the antiferromagnetic ordering, which also leads to a maximum in the negative magnetoresistance at T^* . The conduction mechanism transition at T^* was observed in multiple films of varying thickness, substrate, and composition, confirming the relative insensitivity of the transport mechanisms to thickness, strain, and off-stoichiometry. These results provide new insight into coupled charge/spin ordering transitions by demonstrating the consequences of unconventional antiferromagnetic ordering on electronic conduction.

ACKNOWLEDGMENTS

We are grateful to Chris Leighton and Eun Ju Moon for useful discussions. We thank Phil Ryan and Jong-Woo Kim for assistance with the synchrotron diffraction measurement, Jacob Donius for growing sample JD16, and Leszek Wielunski and Boris Yakshinskiy at the Laboratory for Surface Modification at Rutgers University for performing the RBS measurements. This work was supported by the Office of Naval Research under Grant No. N00014-11-1-0664. Acquisition of the PPMS was supported by the Army Research Office under DURIP Grant No. W911NF-11-1-0283. Use of the Advanced Photon Source, an Office of Science User Facility operated for the U.S. Department of Energy (DOE) Office of Science by Argonne National Laboratory, was supported by the U.S. DOE under Contract No. DE-AC02-06CH11357.

- ¹M. Imada, A. Fujimori, and Y. Tokura, *Rev. Mod. Phys.* **70**, 1039 (1998).
- ²C. N. R. Rao, A. Arulraj, A. K. Cheetham, and B. Raveau, *J. Phys.: Condens. Matter* **12**, R83 (2000).
- ³H. Park, A. J. Millis, and C. A. Marianetti, *Phys. Rev. Lett.* **109**, 156402 (2012).
- ⁴A. Cammarata and J. M. Rondinelli, *Phys. Rev. B* **86**, 195144 (2012).
- ⁵G. Catalan, R. M. Bowman, and J. M. Gregg, *Phys. Rev. B* **62**, 7892 (2000).
- ⁶R. Scherwitzl, P. Zubko, I. G. Lezama, S. Ono, A. F. Morpurgo, G. Catalan, and J.-M. Triscone, *Adv. Mater.* **22**, 5517 (2010).
- ⁷S. Asanuma, P.-H. Xiang, H. Yamada, H. Sato, I. H. Inoue, H. Akoh, A. Sawa, K. Ueno, H. Shimotani, H. Yuan, M. Kawasaki, and Y. Iwasa, *Appl. Phys. Lett.* **97**, 142110 (2010).
- ⁸S. D. Ha, B. Viswanath, and S. Ramanathan, *J. Appl. Phys.* **111**, 124501 (2012).
- ⁹J. Jeong, N. Aetukuri, T. Graf, T. D. Schladt, M. G. Samant, and S. S. P. Parkin, *Science* **339**, 1402 (2013).
- ¹⁰A. Kar, N. Shukla, E. Freeman, H. Paik, H. Liu, R. Engel-Herbert, S. S. N. Bhardwaja, D. G. Schlom, and S. Datta, *Appl. Phys. Lett.* **102**, 072106 (2013).
- ¹¹J. Y. Zhang, J. Hwang, S. Raghavan, and S. Stemmer, *Phys. Rev. Lett.* **110**, 256401 (2013).
- ¹²C. Zhou, D. M. Newns, J. A. Misewich, and P. C. Pattnaik, *Appl. Phys. Lett.* **70**, 598 (1997).

- ¹³J. Son, S. Rajan, S. Stemmer, and S. J. Allen, *J. Appl. Phys.* **110**, 084503 (2011).
- ¹⁴W. L. Lim, E. J. Moon, J. W. Freeland, D. J. Meyers, M. Kareev, J. Chakhalian, and S. Urazhdin, *Appl. Phys. Lett.* **101**, 143111 (2012).
- ¹⁵Y. Zhou and S. Ramanathan, *Crit. Rev. Solid State Mater. Sci.* **38**, 286 (2013).
- ¹⁶J. B. Torrance, P. Lacorre, A. I. Nazzal, E. J. Ansaldo, and C. Niedermayer, *Phys. Rev. B* **45**, 8209 (1992).
- ¹⁷P. Schiffer, A. P. Ramirez, W. Bao, and S.-W. Cheong, *Phys. Rev. Lett.* **75**, 3336 (1995).
- ¹⁸Y. Tomioka, A. Asamitsu, H. Kuwahara, Y. Moritomo, and Y. Tokura, *Phys. Rev. B* **53**, R1689 (1996).
- ¹⁹J.-S. Zhou, J. B. Goodenough, B. Dabrowski, P. W. Klamut, and Z. Bukowski, *Phys. Rev. B* **61**, 4401 (2000).
- ²⁰T. Takeda, R. Kanno, Y. Kawamoto, M. Takano, S. Kawasaki, T. Kamiyama, and F. Izumi, *Solid State Sci.* **2**, 673 (2000).
- ²¹S. K. Park, T. Ishikawa, Y. Tokura, J. Q. Li, and Y. Matsui, *Phys. Rev. B* **60**, 10788 (1999).
- ²²M. Takano, J. Kawachi, N. Nakanishi, and Y. Takeda, *J. Solid State Chem.* **39**, 75 (1981).
- ²³J. Q. Li, Y. Matsui, S. K. Park, and Y. Tokura, *Phys. Rev. Lett.* **79**, 297 (1997).
- ²⁴J. Herrero-Martin, G. Subias, J. Garcia, J. Blasco, and M. Concepción Sánchez, *Phys. Rev. B* **79**, 045121 (2009).
- ²⁵J. Okamoto, D. J. Huang, K. S. Chao, S. W. Huang, C.-H. Hsu, A. Fujimori, A. Masuno, T. Terashima, M. Takano, and C. T. Chen, *Phys. Rev. B* **82**, 132402 (2010).
- ²⁶P. Battle, T. Gibb, and P. Lightfoot, *J. Solid State Chem.* **84**, 271 (1990).
- ²⁷J. Matsuno, T. Mizokawa, A. Fujimori, Y. Takeda, S. Kawasaki, and M. Takano, *Phys. Rev. B* **66**, 193103 (2002).
- ²⁸J. Blasco, B. Aznar, J. García, G. Subías, J. Herrero-Martin, and J. Stankiewicz, *Phys. Rev. B* **77**, 054107 (2008).
- ²⁹R. J. McQueeney, J. Ma, S. Chang, J.-Q. Yan, M. Hehlen, and F. Trouw, *Phys. Rev. Lett.* **98**, 126402 (2007).
- ³⁰J. Ma, J.-Q. Yan, S. O. Diallo, R. Stevens, A. Llobet, F. Trouw, D. L. Abernathy, M. B. Stone, and R. J. McQueeney, *Phys. Rev. B* **84**, 224115 (2011).
- ³¹N. Hayashi, T. Terashima, and M. Takano, *J. Mater. Chem.* **11**, 2235 (2001).
- ³²W. Prellier and B. Mercey, *J. Phys. D: Appl. Phys.* **35**, L48 (2002).
- ³³K. Ueno, A. Ohtomo, F. Sato, and M. Kawasaki, *Phys. Rev. B* **73**, 165103 (2006).
- ³⁴H. Wadati, D. Kobayashi, H. Kumigashira, K. Okazaki, T. Mizokawa, A. Fujimori, K. Horiba, M. Oshima, N. Hamada, M. Lippmaa, M. Kawasaki, and H. Koinuma, *Phys. Rev. B* **71**, 035108 (2005).
- ³⁵T. Ishikawa, S. K. Park, T. Katsufuji, T. Arima, and Y. Tokura, *Phys. Rev. B* **58**, R13326 (1998).
- ³⁶H. Yamada, M. Kawasaki, and Y. Tokura, *Appl. Phys. Lett.* **80**, 622 (2002).
- ³⁷Y. Xie, M. D. Scafetta, R. J. Sichel-Tissot, E. J. Moon, R. C. Devlin, H. Wu, A. L. Krick, and S. J. May, *Adv. Mater.* **26**, 1434 (2014).
- ³⁸E. Breckenfeld, N. Bronn, J. Karthik, A. R. Damodaran, S. Lee, N. Mason, and L. W. Martin, *Phys. Rev. Lett.* **110**, 196804 (2013).
- ³⁹M. Björck and G. Andersson, *J. Appl. Crystallogr.* **40**, 1174 (2007).
- ⁴⁰R. J. Sichel-Tissot, R. C. Devlin, P. J. Ryan, J.-W. Kim, and S. J. May, *Appl. Phys. Lett.* **103**, 212905 (2013).
- ⁴¹M. Jaime, H. T. Hardner, M. B. Salamon, M. Rubinstein, P. Dorsey, and D. Emin, *Phys. Rev. Lett.* **78**, 951 (1997).
- ⁴²T. Holstein, *Ann. Phys.* **8**, 343 (1959).
- ⁴³N. Mott, *J. Non-Cryst. Solids* **1**, 1 (1968).
- ⁴⁴A. Efros and B. I. Shklovskii, *J. Phys. C: Solid State Phys.* **8**, L49 (1975).
- ⁴⁵I. G. Austin and N. F. Mott, *Adv. Phys.* **50**, 757 (2001).
- ⁴⁶S. Tajima, A. Masaki, S. Uchida, T. Matsuura, K. Fueki, and S. Sugai, *J. Phys. C: Solid State Phys.* **20**, 3469 (1987).
- ⁴⁷M. Morishita and H. Yamamoto, *Mater. Trans.* **48**, 3109 (2007).
- ⁴⁸A. Banerjee, S. Pal, and B. K. Chaudhuri, *J. Chem. Phys.* **115**, 1550 (2001).
- ⁴⁹M. Ziese and C. Srinithiwarawong, *Phys. Rev. B* **58**, 11519 (1998).
- ⁵⁰A. Banerjee, S. Pal, S. Bhattacharya, B. K. Chaudhuri, and H. D. Yang, *Phys. Rev. B* **64**, 104428 (2001).
- ⁵¹W. H. Jung and E. Iguchi, *J. Phys.: Condens. Matter* **7**, 1215 (1995).
- ⁵²H. Zhou and J. Goodenough, *J. Solid State Chem.* **178**, 3679 (2005).
- ⁵³V. N. Bogomolov and D. N. Mirlin, *Phys. Status Solidi B* **27**, 443 (1968).
- ⁵⁴C. Ruscher, E. Salje, and A. Hussain, *J. Phys. C: Solid State Phys.* **21**, 3737 (1988).
- ⁵⁵E. Salje and B. Güttler, *Philos. Mag. B* **50**, 607 (1984).
- ⁵⁶K. A. Müller, G.-M. Zhao, K. Conder, and H. Keller, *J. Phys.: Condens. Matter* **10**, L291 (1998).
- ⁵⁷R. Menon, C. O. Yoon, D. Moses, A. J. Heeger, and Y. Cao, *Phys. Rev. B* **48**, 17685 (1993).
- ⁵⁸X. Zhang, M. Manno, A. Baruth, M. Johnson, E. S. Aydil, and C. Leighton, *ACS Nano* **7**, 2781 (2013).
- ⁵⁹K. Shimakawa and K. Miyake, *Phys. Rev. Lett.* **61**, 994 (1988).
- ⁶⁰K. Shimakawa, *Phys. Rev. B* **39**, 12933 (1989).
- ⁶¹L. R. Wienkes, C. Blackwell, and J. Kakalios, *Appl. Phys. Lett.* **100**, 072105 (2012).
- ⁶²J. Kakalios, *J. Non-Cryst. Solids* **114**, 372 (1989).
- ⁶³Y. M. Gal'perin, E. P. German, and V. G. Karpov, *Sov. Phys. JETP* **72**, 193 (1991).
- ⁶⁴S.-W. Cheong, H. Hwang, B. Batlogg, A. Cooper, and P. Canfield, *Physica B* **194–196**, 1087 (1994).
- ⁶⁵S. D. Ha, R. Jaramillo, D. M. Silevitch, F. Schoofs, K. Kerman, J. D. Baniecki, and S. Ramanathan, *Phys. Rev. B* **87**, 125150 (2013).
- ⁶⁶See supplementary material at <http://dx.doi.org/10.1063/1.4883541> for fits to the transport models.